JOURNAL OF THE AMERICAN CHEMICAL SOCIETY
Article
pubs.acs.org/JACS

Synthesis of Nonspherical Superparamagnetic Particles: *In Situ* Coprecipitation of Magnetic Nanoparticles in Microgels Prepared by Stop-Flow Lithography

Su Kyung Suh, Kai Yuet, Dae Kun Hwang,[†] Ki Wan Bong, Patrick S. Doyle,* and T. Alan Hatton*

Department of Chemical Engineering, Massachusetts Institute of Technology, Cambridge, Massachusetts 02139, United States

Supporting Information

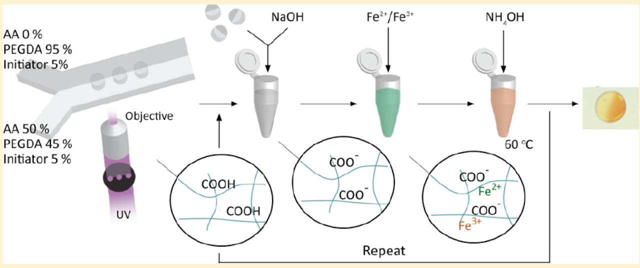

ABSTRACT: We present the synthesis of nonspherical magnetic microparticles with multiple functionalities, shapes, and chemistries. Particle synthesis was performed in two steps: polymeric microparticles functionalized homogenously with carboxyl groups were generated using stop-flow lithography, and then *in situ* coprecipitation was used to grow magnetic nanoparticles at these carboxyl sites. With successive growth of magnetic nanoparticles, we obtained polymeric particles with saturation magnetizations of up to 42 emu/g microparticle. The growth in the magnetic nanoparticle mean size and polydispersity was determined from the magnetization curves obtained following each growth cycle; nanoparticle sizes were limited by the physical constraint of the effective mesh within the hosting gel microparticle. Particles with spatially segregated domains of varying magnetic properties (e.g., Janus particles, particles with step changes in magnetite concentration, etc.) can be synthesized readily using this approach.

INTRODUCTION

Magnetic particles are of increasing interest because of their potential use in various fields such as magnetic separations,[1−3] catalysis,[4] biomedical applications,[5,6] and data storage.[7] These applications are enabled by the ability to manipulate the particles using external magnetic fields. For the precise control of the particles, superparamagnetism is advantageous over ferromagnetism, as superparamagnetic particles have an oriented magnetic moment under a magnetic field but lose this property in the absence of the field; i.e., they do not exhibit remanence or hysteresis. Therefore, we expect to observe a consistent response from superparamagnetic materials to an imposed field, in contrast to the anticipated variable response from ferromagnetic particles. Ferromagnetic materials can be superparamagnetic when they have single domains, typically with small particles of size less than about 20 nm.[8] However, since the magnetic force on a particle is proportional to its volume, large particles are more easily manipulated than are small particles by external magnetic fields. As such, the synthesis of large, superparamagnetic particles is desirable for many applications such as those mentioned above.

Large paramagnetic particles can be prepared by assembling superparamagnetic nanoparticles into stable aggregates, or by dispersing such magnetic nanoparticles throughout a particle matrix. The first approach utilizes the clustering of nanoparticles, which can be achieved via self-assembly of magnetic nanoparticles[9−11] or the use of emulsions as templates.[12−14] Further coating or functionalization of these clusters can be realized as required for specific applications, and if desired, composite particles can be prepared with magnetic nanoparticle clusters constituting either the cores or the shells of core−shell particles.[14−18] The second approach relies on the incorporation of magnetic nanoparticles within porous structures, through either growth of nanoparticles[19−22] or their direct entrapment[23,24] within polymer matrices. While magnetic nanoparticle clusters tend to exhibit higher saturation magnetization than do polymer-based paramagnetic particles due to higher magnetic material densities, polymer substrates provide greater flexibility in terms of chemical functionality and mechanical properties.

The ability to prepare superparamagnetic particles with precise control over particle morphology is desirable for many applications. For instance, induced mechanical stresses on magnetic particles can be controlled by external magnetic fields, and thus magnetic particles with various shapes enable the study of simplified versions of complex systems.[14,25,26] Also, nonspherical magnetic particles introduce magnetic anisotropies, which allow the assembly of complex structures such as flowers, double helices, and zigzag chains.[27−31] With the ability to control the shapes and functionalities of the building blocks used for assembly, the interaction between the components can be engineered precisely. To date, the synthesis of nonspherical magnetic particles has been achieved primarily using soft lithography in the presence of magnetic nanoparticles.[32−35] Unfortunately, magnetic nanoparticles absorb a considerable fraction of the incident UV irradiation used to cure the particles, and thus, the number of magnetic nanoparticles that

Received: September 30, 2011
Published: March 30, 2012

dx.doi.org/10.1021/ja209245v | *J. Am. Chem. Soc.* 2012, 134, 7337−7343

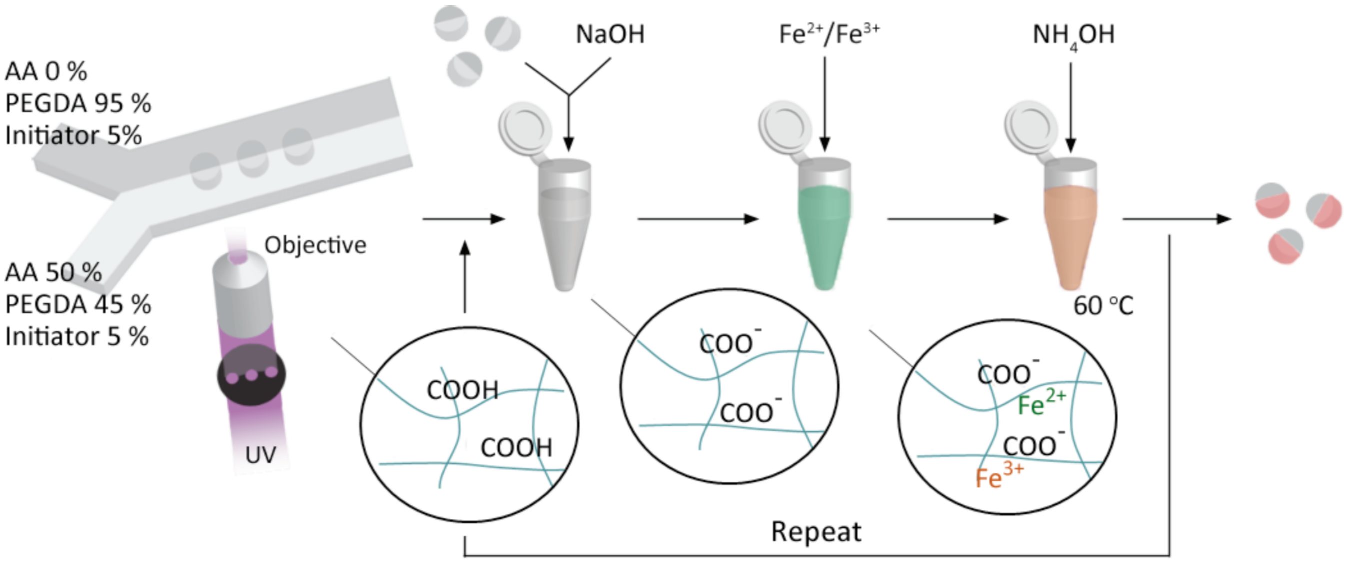

Figure 1. Schematic showing the synthesis process.

can be incorporated successfully into the polymeric particles is limited.

As particles with lower magnetization require higher magnetic fields to yield reasonable response times, it is desirable to create particles with the greatest possible superparamagnetic properties. Here, we demonstrate a versatile method to generate complex, nonspherical magnetic particles with high magnetization. Hydrogel particles with configurable shapes and chemistries can be created via stop-flow lithography (SFL).[36] Using SFL, we synthesized polymeric particles bearing carboxyl groups capable of capturing ferric and ferrous ions which were then coprecipitated to form magnetic nanoparticles embedded within the polymeric particle matrices. We generated multifunctional particles of varying magnetic content by successive growth of magnetic nanoparticles within the gel matrices, and this procedure can be used to increase the saturation magnetization to as high as 42 emu/g microparticle. The mechanism of successive growth has been elucidated to explain the increase in saturation magnetization of both nanoparticles and polymer/nanoparticle composites.

■ EXPERIMENTAL SECTION

Materials. Polymeric particles are prepared using poly(ethylene glycol) (700) diacrylate (PEG-DA 700, Sigma-Aldrich), acrylic acid (AA, Sigma-Aldrich), and 2-hydroxy-2-methylpropiophenon (Darocur 1173, Sigma-Aldrich) initiator. Tween-20 (Sigma Aldrich) was used at 0.05% to prevent particle loss due to sticking on pipet tips or tubes. To synthesize magnetic nanoparticles, we used ferric chloride hexahydrate ($FeCl_3 \cdot 6H_2O$, Sigma Aldrich), ferrous chloride tetrahydrate ($FeCl_2 \cdot 4H_2O$, Sigma Aldrich), sodium hydroxide (NaOH, Sigma Aldrich), and ammonium hydroxide (NH_4OH, Sigma Aldrich).

Microfluidic Device Fabrication. Microfluidic devices for SFL were fabricated with polydimethyl-siloxane elastomer (PDMS, Sylgard 184, Dow Corning) mixed at a ratio of 10:1 base to curing agent. The PDMS microchannels were molded by pouring elastomer on a patterned silicon wafer (SU-8 photoresist, Microchem) and baking in an oven at 65 °C for 2 h. PDMS-coated glass slides used for the bottom of the devices were prepared by spreading a thin layer of elastomer on a slide and curing partially at 65 °C for 22 min. The clean PDMS patterns from the wafer were assembled with the glasses and were kept in the oven for 45 min. The prepared microfluidic channel was assembled with inlets that were made of pipet tips (ART 10 Reach and ART 200, Molecular BioProducts, Inc.) and outlet aluminum tubing (1/16 in., K&S) for collecting particles after synthesis. For particle synthesis, the channels were placed on an inverted microscope (Axiovert 200, Zeiss).

Stop-Flow Lithography Setup. We polymerized microparticles of the desired shapes and chemistries when flow was stopped in the microfluidic device. Then, particles were pushed out of the polymerization area with flow of the monomer solutions. This stop−expose−flow cycle was commanded by a custom script that toggled a solenoid valve (Burkert) to control the inlet pressure on the monomer streams from 0 to 3 psi and opened or closed a UV shutter (VS25, UniBlitz). Monomer solutions were polymerized with the UV source of Lumen 200 (Prior Scientific, 100% setting). A UV filter (11000v2, Chroma) was used to provide the desired excitation for polymerization. Transparency masks (Bandon, OR) designed in AUTOCAD 2005 were used to shape the UV illumination used for particle synthesis. For multiple inlets, the thicknesses of the inlet streams were controlled by a pressure valve (ControlAir, Inc.) in response to readings from a digital pressure gauge (DPG 100G, Omega Engineering, Inc.).

Polymeric Particle Synthesis. Homogenous microparticles were prepared from oligomer solutions consisting of 50% (v/v) AA, 45% (v/v) PEG-DA 700, and 5% (v/v) Darocur 1173. The Janus particles were obtained using two monomer solutions, one with 50% (v/v) AA, 45% (v/v) PEG-DA 700, and 5% (v/v) Darocur 1173 and the other with 45% (v/v) PEG-DA 700, 5% (v/v) Darocur 1173, and 50% (v/v) water. For the preparation of multicompartmented particles, our inlet solutions contained 0%, 15%, 30%, and 45% (v/v) of AA, and 50%, 35%, 20%, and 5% (v/v) of water, respectively, in the monomer solutions. The polymerization time was 75 ms for all particles.

***In-Situ* Magnetic Nanoparticle Synthesis.** The schematic diagram in Figure 1 shows the coprecipitation process. The clean polymer particles were dispersed in 0.5 M NaOH solution for 10 min to deprotonate the COOH groups to COO^-. Particles with COO^- were washed 5 times with 0.5% Tween 20 solution to reach neutral pH. 0.2 M $FeCl_3$, and 1 M $FeCl_2$ solutions were prepared in N_2 purged water and mixed with the polymer particles to meet the desired ratio of Fe^{3+}:Fe^{2+} = 1:75. After iron ions diffused into the polymer particles and were allowed to chelate with the deprotonated carboxyl groups for 30 min, the excess iron salts were removed. Following adjustment of the pH with NH_4OH at 60 °C, magnetic nanoparticles nucleated and grew in the polymer particles. The magnetic microparticles were rinsed 5 times with Tween 20 solutions. For successive growth, the steps from the deprotonation step were repeated.

Characterizations. The magnetization of particles under an applied magnetic field was measured using a superconducting quantum interference device (SQUID, MPMS-5S, Quantum Design). All

SQUID measurements were performed at 300 K over the magnetic field range 0−5 T on 1−3 mg of dried particles. Transmission electron microscopy (TEM, 200-CX, JEOL) images were obtained at 200 kV. The samples were prepared by placing thinly sliced particles on lacey carbon-coated 200 mesh copper grids (Electron Microscopy Sciences). Dried microparticles were cured in epoxy (Sigma Aldrich) for 24 h and were sliced with a Microtome (MT-X, Ultra Microtome) to give 40 nm thick samples. Scanning electron microscopy (SEM, 6060, JEOL) was used to analyze the surfaces of dried particles. Samples were prepared by dropping 10 μL of particle solution on the glass slides.

■ RESULTS AND DISCUSSION

We demonstrated the synthesis of magnetic microparticles using *in situ* growth of nanoparticles in polymer particles preformed by SFL. Our approach provides a versatile, inexpensive method for obtaining multifunctional and nonspherical magnetic particles with strong magnetic properties. The PEG/PAA polymeric particles investigated in this study were synthesized using SFL as shown in Figure 1. We blended acrylic acid with the PEG monomer precursor in order to introduce anionic carboxyl groups in the polymeric particle substrate, which could act as iron ion binding sites for nanoparticle growth. We also generated Janus particles using SFL with two monomer streams (Figure 1); the top stream was composed of PEG-DA and photoinitiator, while the bottom stream included PEG-DA, AA, and photoinitiator. These Janus particles enabled selective adsorption of ions in one region of the particles only.

To create nanoparticles in the polymer gel matrices generated using SFL, the gels were suspended in a sodium hydroxide solution for the deprotonation of the COOH groups to COO^-. Electrostatic repulsion between these charged groups increased the osmotic pressure within the gel, causing the PEG/PAA particle substrate to swell. Then, these anionic polymer particles were mixed with solutions of ferrous and ferric ions. In order to create magnetite instead of other iron oxides that have low magnetizations, precise control of the Fe^{3+}/Fe^{2+} ratio was necessary. The Fe^{3+} ion is attracted to carboxyl groups more strongly than is Fe^{2+}, and thus, the bulk solution was prepared with an Fe^{3+}/Fe^{2+} ratio of 1:75 to ensure an Fe^{3+}/Fe^{2+} ratio of approximately 2 within the polymer particles, as needed to produce magnetite nanoparticles.[37] This optimum ratio was selected because it gave the highest saturation magnetization of the final particles, as discussed in the Supporting Information. The polymeric particles were dispersed in the solution for 30 min during which period the iron ions diffused into them and chelated with the carboxyl ions. With typical particle dimensions (L) of 15 μm and diffusivities (D) of iron ions through the gel substrate of 0.5×10^{-9} m^2/s,[38] the diffusion time scale ($\tau = L^2/D \sim 1$ s) was much shorter than the incubation time so that the ferric and ferrous ions were able to penetrate the full depth of the particles. The pH was adjusted by adding NH_4OH, and the temperature was held at 60 °C for 15 min during magnetite deposition. These processes created magnetite with bare surfaces entrapped in the polymer particles.

We generated nonspherical magnetic particles in the shapes of disks and triangles as shown in Figure 2a,b. The morphology of the particles was dictated by the mask used to shape the UV light beam prior to its introduction to the microfluidic channel during SFL. Various sizes of particles from 20 (Figure S2) to 300 μm could be created by changing the mask size. In this manner, particles of virtually any extruded two-dimensional shape can be created. With multiple coflowing monomer streams, this method can also be used to generate multifunctional particles. The Janus magnetic particles shown in Figure 2c were obtained by adding acrylic acid to just one of two inlet streams. The brown magnetic region in the final particles is clearly distinguishable from the inert PEG region, as the synthesis of magnetite occurred only in the presence of the carboxyl groups. Furthermore, our ability to incorporate various chemistries in a single particle with SFL enables the synthesis of particles with spatially varying magnetic properties. Using four inlets with monomers containing different concentrations of acrylic acid from 0% to 45%, particles were prepared with step changes in iron oxide content, as shown in Figure 2d.

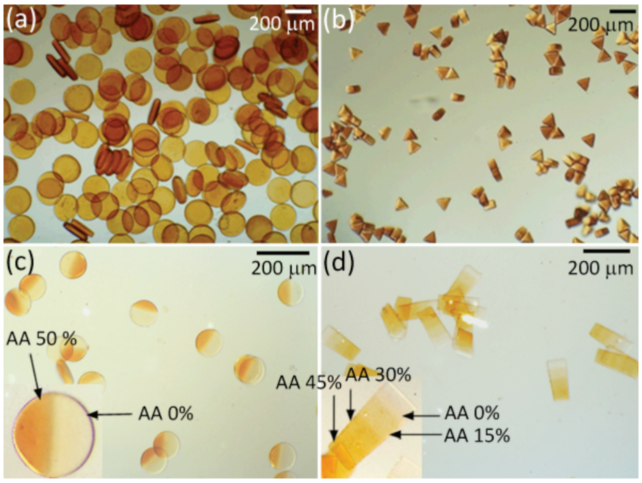

Figure 2. Optical images of various magnetic microparticles: (a) homogenous magnetic disks, (b) homogenous tranglular particles, (c) Janus disks, (d) gradient particles.

Since magnetic functionalization is not perfectly efficient with respect to the active groups within the hydrogel, carboxyl groups remain in the particles after the magnetite nucleation and synthesis. The growth of nanoparticles, shown schematically in Figure 1, can be repeated several times to increase magnetic properties. Figure 3 contains optical images of microparticles subjected to several cycles of magnetic nanoparticle synthesis, in which the color of the particles becomes darker as the number of cycles increases and opaque particles are generated containing more magnetic nanoparticles.

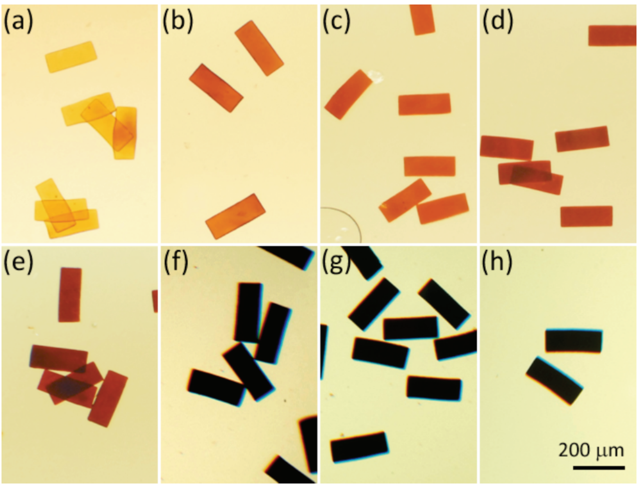

Figure 3. Successive synthesis of magnetite in micro-polymer-particles.

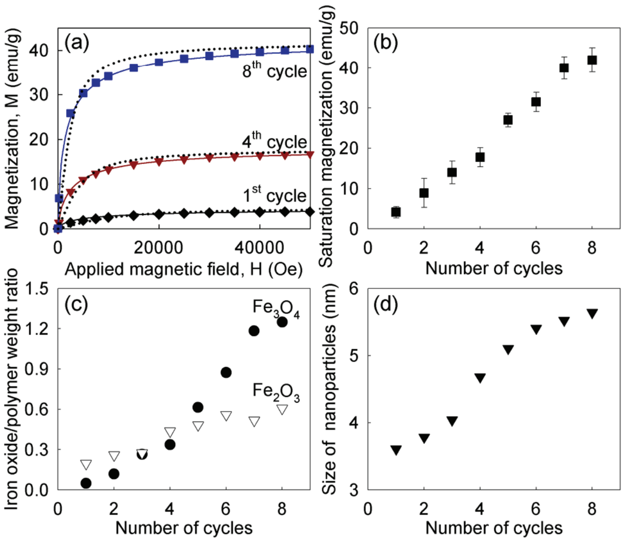

Figure 4. Magnetic properties of magnetic microparticles and nanoparticles. (a) Magnetization curves. The points were obtained from SQUID measurement, while solid lines were calculated using Chantrell's method shown in eq 6. The dotted line was obtained from the Langevin function assuming that particles were monodisperse. (b) Saturation magnetization values of polymer/nanoparticle complexes. (c) Magnetic nanoparticle content excluding the polymer matrix calculated using results in panel b and TGA analysis. The ratios $x_{\mathrm{Fe3O4}}/x_{\mathrm{PEG/PAA}}$ and $x_{\mathrm{Fe2O3}}/x_{\mathrm{PEG/PAA}}$ are plotted. (d) Nanoparticle sizes calculated using Chantrell's method.

In order to determine the magnetic properties of the particles following each cycle, we obtained magnetization curves from SQUID measurements, as shown in Figure 4a. All magnetic particles exhibited superparamagnetism without remanence. The magnetization M of an assembly of monodisperse superparamagnetic nanoparticles of diameter d in the direction of an applied magnetic field H can be described by the Langevin function

$$\frac{M}{\phi M_d} = \coth \alpha - \frac{1}{\alpha} \equiv L(\alpha) \qquad (1)$$

where ϕ is the solid volume fraction, M_d is the saturation magnetization of the bulk material based on volume, $\alpha = \pi\mu_0 M_d H d^3/6kT$, k is the Boltzmann constant, T is the temperature, and μ_0 is the permeability of free space.[8]

Nanoparticles synthesized by chemical coprecipitation are generally not monodisperse, however, and it is typically assumed that these magnetic nanoparticles follow a log-normal distribution in size,[39,40] with the probability density function given by

$$P(x) = \frac{1}{\sqrt{2\pi}\,\sigma x} e^{-(\ln x-\mu)^2/2\sigma^2} \qquad (2)$$

where $x = D/D_p$ is the reduced diameter, μ is the mean of ln x, D_p is the median diameter, and σ is the standard deviation of the log-normal distribution.

The magnetization curve for a polydispersed collection of nanoparticles can be obtained by integrating the Langevin function over the particle size distribution to obtain

$$M(\alpha) = \frac{\pi}{6} M_d D_p^{\,3} \int_0^\infty L(\alpha) x^3 P(x)\, dx \qquad (3)$$

Under high applied magnetic fields, this equation reduces to

$$M = \phi M_d \left(1 - \left[\frac{6}{\pi} \frac{kT}{\mu_0 M_d D_p^{\,3}} \int_0^\infty x^{-3} P(x)\, dx \right] \frac{1}{H} \right) \qquad (4)$$

According to this equation, the saturation magnetization of the nanoparticles, $M_s = \phi M_d$, can be obtained from the intercept of the M versus inverse H plot of the data at large values of H. Assuming that we created mostly magnetite and not other oxides, we used M_d = 92 emu/g.[41] As was expected, the saturation magnetization of microparticles (Figure 4b) increased with an increasing number of cycles without loss of nanoparticles during the deprotonation of the carboxyl groups with NaOH. The saturation magnetization reached 42 emu/g after eight cycles. This value is on the high end for typical commercially available magnetic beads, which have saturation magnetizations in the range 20−40 emu/g.

The magnetization curves also yielded the average diameter and size distribution of the magnetic nanoparticles. Chantrell et al. showed that the median diameter (D_p) and standard deviation (σ) of magnetic nanoparticles distributed according to the log-normal distribution can be obtained from the magnetization curves using[39]

$$D_p = \left(\frac{18kT}{\pi M_d} \left[\frac{\chi_i}{3\phi M_d H'} \right]^{1/2} \right)^{1/3} \qquad (5)$$

$$\sigma = \frac{1}{3} \left(\ln\left(\frac{3\chi_i H'}{\phi M_d} \right) \right)^{1/2} \qquad (6)$$

where χ_i is the initial magnetic susceptibility and H' is obtained from the M = 0 intercept of a graph of M versus $1/H$ at high applied field strength. Diameters of nanoparticles calculated in this manner are shown in Figure 4d as a function of repetition cycle number, where it is evident that the particle size increased with successive nanoparticle synthesis cycle as we loaded more magnetite into the polymer particles. Magnetite can be grown either on the surfaces of existing nanoparticles or at unoccupied carboxyl groups to form new nucleation points. Nanoparticle diameter did not increase as significantly at low cycle numbers as it did in the later cycles, leading to the conclusion that, at low cycle numbers, the nucleation of new nanoparticles at unoccupied carboxyl sites is the dominant form of magnetite incorporation. We note that the diameter of nanoparticles reached approximately 5.7 nm. The nanoparticle size cannot exceed the mesh size in polymer particles, since the mesh exerts physical constraints on nanoparticle growth. Hence, the maximum particle size is close to the mesh size of swollen polymer particles. The σ of nanoparticles varied from 0.32 to 0.43, increasing with the synthesis repetition cycle number. The higher values of σ obtained in the later cycles imply that successive synthesis produced a wider range of particle sizes owing to both nucleation and growth occurring during the nanoparticle synthesis process. We believe that this range of polydispersity is acceptable as coprecipitation is notorious for imprecise size control.

Using the parameter values estimated for H, D_p, and σ from the experimental data in eq 3, we calculated the magnetization curve over the entire range of H values of interest and compared them to the experimental data, as shown in Figure 4a. The predictions are excellent over the full range of H values employed in the experiments (solid lines), in contrast to the best fit profiles obtained if the distribution were assumed to be monodispersed (broken lines), validating the assumption of a log-normal distribution for describing the magnetic nanoparticle size distribution.

We performed TEM analysis to further characterize the magnetic nanoparticles within the hydrogel matrix of the microparticles. The microparticle samples were prepared as thin slices with a thickness of 40 nm using a Microtome. As shown in Figure 5, the nanoparticles grown within the polymeric matrix were distributed uniformly indicating that the carboxyl groups effectively attracted iron ions from the bulk into the polymer particles. Figure 5a,b shows the effect of successive synthesis of magnetite, with respect to both nucleation and growth. Consistent with our expectation that we loaded more magnetite with each successive coprecipitation, Figure 5b with four cycles shows larger particles (4.98 nm) than does Figure 5a with one cycle (3.63 nm). In addition since both samples have the same thickness, the image from the fourth cycle, with a darker appearance, indicates that more magnetite was incorporated into the polymer gels.

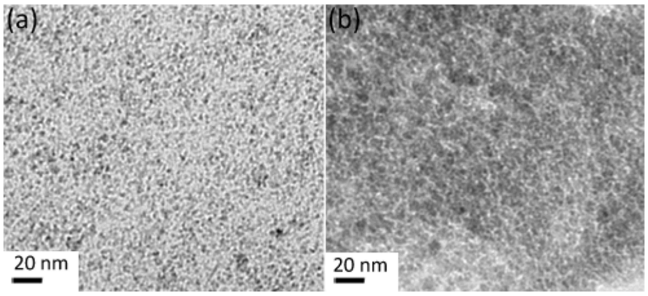

Figure 5. Cross-sectional TEM images of magnetite/polymer matrix. Magnetic nanoparticles in polymeric particles after (a) the first cycle and (b) the fourth cycle.

The diameters of nanoparticles shown in Figure 4d are smaller than those in Figure 5. This can be explained by investigating Chantrell's method for calculation of particle size. The saturation magnetization value used in this calculation is that of bulk magnetite. However, as magnetic nanoparticles usually have a magnetite core and thin shell (0.8 nm) of nonmagnetic material, the corresponding magnetization would be smaller than nanoparticles composed of magnetite only.[7] Therefore, eq 2 underestimates the size of nanoparticles.

By exploring the saturation magnetization of particles and the weight content of total iron oxide, we can estimate the amount of magnetite (Fe_3O_4) and antiferromagnetic iron oxide (α-Fe_2O_3) in the polymeric particles. The TGA results provide the weight fraction of the PEG and PAA polymers comprising the particle, as polymers burn at high temperature (~600 °C). The balance equations

$$x_{\mathrm{PEG/PAA}} + x_{\mathrm{Fe_3O_4}} + x_{\alpha\text{-}\mathrm{Fe_2O_3}} = 1 \tag{7}$$

and

$$\mathbf{M_d} x_{\mathrm{Fe_3O_4}} = \mathbf{M_s} \tag{8}$$

where x is the weigh fraction of each component, can be used to determine the magnetite fraction in the particles. The calculated results are shown in Figure 4c. Microparticles contained more Fe_2O_3 than Fe_3O_4 after the first and second synthesis of nanoparticles, but the weight percent of Fe_3O_4 exceeded that of Fe_2O_3 beyond the fourth synthesis. Although the preferential synthesis of Fe_2O_3 in initial synthesis cycles was unexpected, it can be explained by investigation of our synthesis process. Before we increased the pH to precipitate magnetite, we did not wash out the excess iron ions in solution. As the diffusion time scale was short in our porous particles, washing steps rapidly extracted the chelated iron ions in the polymer particles. Therefore, we chose simply to remove the excess iron solution rather than wash the particles in fresh buffer solution. However, this led to the creation of undesired iron oxides, as the bulk iron solution had the ratio of Fe^{2+}:Fe^{3+} = 75:1. With NH_4OH, nonmagnetic iron oxides can be produced both in the bulk solution and on the surfaces of polymeric particles, where the ratio of irons is similar to that in the bulk, as shown schematically in Figure 6. The α-Fe_2O_3, known to be made from Fe^{2+} at high pH, can be attached to the surface of the polymer particles. The color of the solution, which had a light red hue, was consistent with the formation of α-Fe_2O_3.[42]

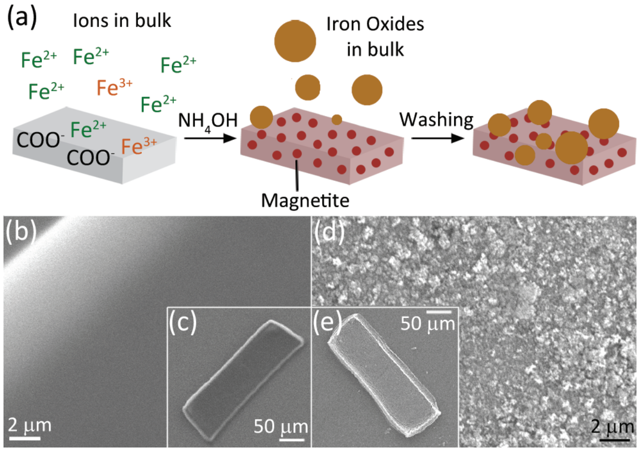

Figure 6. (a) Schematic showing the formation of magnetic nanoparticles in bulk solution and their attachment to the microparticle surface. The ratio between Fe^{2+} and Fe^{3+} ions in bulk is different from that in the polymer matrix. (b) SEM image of PAA/PEG particles. (c) The particle in panel b imaged at low magnification. (d) PAA/PEG/iron oxide particle surfaces. (e) The particle in panel d imaged at low magnification.

The SEM images in Figure 6 indicate that the surfaces of microparticles after magnetic functionalization were not as smooth as those of the parent polymeric particles, but were coated with micrometer-size clusters. Comparison of the TEM images in Figure 5 and the SEM images in Figure 6 indicates that the clusters on the particle surface were different in size and shape than those formed within the microparticle. In addition, iron oxides are cation adsorbents, and thus, iron ions could be attracted to microparticles even though most of the carboxyl groups were occupied with previously synthesized magnetite.

The rapid increase of Fe_3O_4 content with synthesis cycle repetition, as shown in Figure 4c, can be caused by the larger quantity of iron oxide present in polymeric particles with each subsequent growth. However, there is again a physical constraint on the growth of magnetic nanoparticles with the limited mesh size in the polymer particles. Interestingly, the shapes of the curves for Fe_3O_4 in Figure 4c,d are similar, indicating that more cations can be adsorbed with larger nanoparticle size, but that a finite limit on size can be achieved due to mesh size limitations. In contrast to the trend seen for Fe_3O_4, the Fe_2O_3 content does not increase significantly after the first few synthesis cycles. Since Fe_2O_3 would be associated with the surfaces of the polymer particles, addition of Fe_2O_3 to the polymer particles would occur in the early cycles only as the surface quickly became saturated. Also, Fe_2O_3 on polymer particles will be detached when Fe_2O_3 particles are too large to adhere to the surfaces of the hydrogel particles during the washing cycle.

We can also account for the high loading of Fe_2O_3 in lower cycles as thin layers grown over a core of Fe_3O_4. If the shell thickness in 3 nm particles is the same as that in 5 nm particles, the thin shells make up a larger volume fraction of the smaller particles than of the larger particles. In other words, Fe_2O_3 is more abundant with smaller particles in low cycle numbers. In addition, the apparent Fe_2O_3 reflects the disordered layer at the nanoparticle surface, which becomes ordered as the new layers are added.

An alternate approach to making magnetic particles via microfluidic channels is to incorporate commercial magnetic beads (20−40 emu/g) in the monomer mix during synthesis.[30,33,34] As this method usually does not require postsynthesis functionalization, one might assume that it would be a faster and simpler means to generate magnetic particles. However, the final magnetization of the polymeric particles prepared by this method will be considerably lower than that of the magnetic beads owing to the extra mass added by the polymeric substrate. For photopolymerization, the presence of these opaque magnetic beads also makes polymerization challenging due to attenuation and limited penetration of the light into the reaction mixture because of absorbance by the beads. Hence, many reported superparamagnetic microparticles generated photochemically using direct incorporation of magnetic materials have typical magnetization values of 5 emu/g or less due to limitations on magnetic loading. On the contrary, using our postfunctionalization approach, we controlled not only the shape of particles but also the extent of functionalization, achieving saturation magnetizations of up to 42 emu/g, using successive growth.

■ CONCLUSION

In conclusion, we demonstrate the synthesis of nonspherical magnetic microparticles via stop-flow lithography and *in situ* magnetic nanoparticle synthesis. The method described here allows for the synthesis of multifunctional and highly magnetic particles depending on the number of successive nanoparticle synthesis cycles used. We investigated the properties of the particles on both microscopic and nanoscopic scales, elucidating the mechanism of the synthesis process. The synthesis is straightforward and can be carried out under relatively low temperature and atmospheric pressure conditions using common chemicals. Also, this study can be adapted to the synthesis of other nanoparticles using coprecipitation, introducing the flexibility to create desired particle shapes with a great range of functionalities. Since particles have unoccupied carboxyl groups even after the first nanoparticle creation, this method can be used to add multiple functionalities, such as the addition of biomolecules, with subsequent reactions.

■ ASSOCIATED CONTENT

Ⓢ Supporting Information

Details on (i) optimization of the iron ion ratio, (ii) X-ray diffraction (XRD) patterns, and (iii) synthesis of smaller particles. This material is available free of charge via the Internet at http://pubs.acs.org.

■ AUTHOR INFORMATION

Corresponding Author

tahatton@mit.edu; pdoyle@mit.edu

Present Address

[†]Department of Chemical Engineering, Ryerson University, Toronto, Ontario M5B 2K3, Canada.

Notes

The authors declare no competing financial interest.

■ ACKNOWLEDGMENTS

This work was supported by Singapore-MIT alliance and in part by NSF Grant DMR-1006147. The assistance of Prof. vander Sande with the TEM analysis is gratefully acknowledged. We thank Patrick Boisver and Dr. Shaoyan Chu for help with microtome and SQUID measurements.

■ REFERENCES

(1) Miltenyi, S.; Muller, W.; Weichel, W.; Radbruch, A. *Cytometry* **1990**, *11*, 231.

(2) Franzreb, M.; Sieman-Herzberg, M.; Hobley, T. J.; Thomas, O. R. T. *Appl. Microbiol. Biotechnol.* **2006**, *70*, 505.

(3) Ditsch, A.; Lindenmann, S.; Laibinis, P. E.; Wang, D. I. C.; Hatton, T. A. *Ind. Eng. Chem. Res.* **2005**, *44*, 6824.

(4) Stevens, P. D.; Fan, J. D.; Gardimalla, H. M. R.; Yen, M.; Gao, Y. *Org. Lett.* **2005**, *7*, 2085.

(5) Gupta, A. K.; Gupta, M. *Biomaterials* **2005**, *26*, 3995.

(6) Mornet, S.; Vasseur, S.; Grasset, F.; Veverka, P.; Goglio, G.; Demourgues, A.; Portier, J.; Pollert, E.; Duguet, E. *Prog. Solid State. Chem.* **2006**, *34*, 237.

(7) Terris, B. D.; Thomson, T. *J. Phys. D: Appl. Phys.* **2005**, *38*, R199.

(8) Rosensweig, R. E. *Ferrohydrodynamics*; Cambridge University Press: Cambridge, U.K., 1985.

(9) Ge, J. P.; Hu, Y. X.; Biasini, M.; Beyermann, W. P.; Yin, Y. D. *Angew. Chem., Int. Ed.* **2007**, *46*, 4342.

(10) Ditsch, A.; Laibinis, P. E.; Wang, D. I. C.; Hatton, T. A. *Langmuir* **2005**, *21*, 6006.

(11) Lattuada, M.; Hatton, T. A. *J. Am. Chem. Soc.* **2007**, *129*, 12878.

(12) Zhuang, J. Q.; Wu, H. M.; Yang, Y. A.; Cao, Y. C. *J. Am. Chem. Soc.* **2007**, *129*, 14166.

(13) Bai, F.; Wang, D. S.; Huo, Z. Y.; Chen, W.; Liu, L. P.; Liang, X.; Chen, C.; Wang, X.; Peng, Q.; Li, Y. D. *Angew. Chem., Int. Ed.* **2007**, *46*, 6650.

(14) Isojima, T.; Suh, S. K.; Sande, J. B. V.; Hatton, T. A. *Langmuir* **2009**, *25*, 8292.

(15) Shang, H.; Chang, W. S.; Kan, S.; Majetich, S. A.; Lee, G. U. *Langmuir* **2006**, *22*, 2516.

(16) Lambert, E. M.; Viravaidya, C.; Li, M.; Mann, S. *Angew. Chem., Int. Ed.* **2010**, *49*, 4100.

(17) Stoeva, S. I.; Huo, F. W.; Lee, J. S.; Mirkin, C. A. *J. Am. Chem. Soc.* **2005**, *127*, 15362.

(18) Bromberg, L.; Chang, E. P.; Hatton, T. A.; Concheiro, A.; Magariños, B.; Alvarez-Lorenzo, C. *Langmuir* **2011**, *27*, 420.

(19) Ugelstad, J.; Berge, A.; Ellingsen, T.; Schmid, R.; Nilsen, T. N.; Mork, P. C.; Stenstad, P.; Hornes, E.; Olsvik, O. *Prog. Polym. Sci.* **1992**, *17*, 87.

(20) Zhang, J. G.; Xu, S. Q.; Kumacheva, E. *J. Am. Chem. Soc.* **2004**, *126*, 7908.

(21) Kroll, E.; Winnik, F. M.; Ziolo, R. F. *Chem. Mater.* **1996**, *8*, 1594.

(22) Bhattacharya, S.; Eckert, F.; Boyko, V.; Pich, A. *Small* **2007**, *3*, 650.

(23) Yang, C. L.; Shao, Q.; He, J.; Jiang, B. W. *Langmuir* **2010**, *26*, 5179.

(24) Hwang, D. K.; Dendukuri, D.; Doyle, P. S. *Lab Chip* **2008**, *8*, 1640.
(25) Dreyfus, R.; Baudry, J.; Roper, M. L.; Fermigier, M.; Stone, H. A.; Bibette, J. *Nature* **2005**, *437*, 862.
(26) Ghosh, A.; Fischer, P. *Nano Lett.* **2009**, *9*, 2243.
(27) Erb, R. M.; Son, H. S.; Samanta, B.; Rotello, V. M.; Yellen, B. B. *Nature* **2009**, *457*, 999.
(28) Zerrouki, D.; Baudry, J.; Pine, D.; Chaikin, P.; Bibette, J. *Nature* **2008**, *455*, 380.
(29) Smoukov, S. K.; Gangwal, S.; Marquez, M.; Velev, O. D. *Soft Matter* **2009**, *5*, 1285.
(30) Chen, C. H.; Abate, A. R.; Lee, D. Y.; Terentjev, E. M.; Weitz, D. A. *Adv. Mater.* **2009**, *21*, 3201.
(31) Lee, S. H.; Liddell, C. M. *Small* **2009**, *5*, 1957.
(32) Nunes, J.; Herlihy, K. P.; Mair, L.; Superfine, R.; DeSimone, J. M. *Nano Lett* **2010**, *10*, 1113.
(33) Bong, K. W.; Chapin, S. C.; Doyle, P. S. *Langmuir* **2010**, *26*, 8008.
(34) Kim, H.; Ge, J.; Kim, J.; Choi, S.; Lee, H.; Lee, H.; Park, W.; Yin, Y.; Kwon, S. *Nat. Photonics* **2009**, *3*, 534.
(35) Yuet, K. P.; Hwang, D. K.; Haghgooie, R.; Doyle, P. S. *Langmuir* **2010**, *26*, 4281.
(36) Dendukuri, D.; Gu, S. S.; Pregibon, D. C.; Hatton, T. A.; Doyle, P. S. *Lab Chip* **2007**, *7*, 818.
(37) Huang, J. S.; Wan, S. R.; Guo, M.; Yan, H. S. *J. Mater. Chem.* **2006**, *16*, 4535.
(38) Easteal, A. J.; Price, W. E.; Woolf, L. A. *J. Phys. Chem.* **1989**, *93*, 7517.
(39) Chantrell, R. W.; Popplewell, J.; Charles, S. W. *IEEE Trans. Magn.* **1978**, *14*, 975.
(40) Shen, L. F.; Laibinis, P. E.; Hatton, T. A. *Langmuir* **1999**, *15*, 447.
(41) Yamaura, M.; Camilo, R. L.; Sampaio, L. C.; Macedo, M. A.; Nakamura, M.; Toma, H. E. *J. Magn. Magn. Mater.* **2004**, *279*, 210.
(42) Cornell, R. M.; Schwertmann, U. *The Iron Oxides: Structure, Properties, Reactions, Occurrences, and Uses*, 2nd, completely revised and extended, ed.; Wiley-VCH: Weinheim, 2003.